



Highly efficient photocatalytic performances of SnO₂-deposited ZnS nanorods based on interfacial charge transfer



Jaewon Lee^{a,1}, Yeonho Kim^{b,1}, Joon Ki Kim^a, Seongchan Kim^a, Dal-Hee Min^a, Du-Jeon Jang^{a,*}

^a Department of Chemistry, Seoul National University, NS60, Seoul 08826, Republic of Korea

^b Division of Electron Microscopic Research, Korea Basic Science Institute, Daejeon 34133, Republic of Korea

ARTICLE INFO

Article history:

Received 29 August 2016

Received in revised form

21 December 2016

Accepted 25 December 2016

Available online 27 December 2016

Keywords:

Charge separation

Decay time

Heterojunction

Photodegradation

Photostability

ABSTRACT

SnO₂/ZnS nanocomposites of SnO₂ quantum dots (QDs)-deposited ZnS nanorods having highly enhanced photocatalytic activity and photostability have been fabricated via a facile two-step hydrazine-assisted hydrothermal process without involving any surface treatments. The photocatalytic activity of SnO₂/ZnS nanocomposites with a Sn-to-Zn molar ratio ($R_{\text{Sn/Zn}}$) of 0.1 is 3 times higher than that of pristine ZnS nanorods and 17 times higher than that of commercial ZnS. The incorporation of SnO₂ QDs increases the photocatalytic efficiency of ZnS nanorods due to the following reasons: photogenerated charge carriers are readily separated owing to type II band configuration and direct contact at interfaces without having any linker molecules; active surface sites are increased to adsorb more dye molecules; the light absorption range is extended to the visible region, generating more charge carriers on the surfaces of heterojunction structures. The decay time, as well as the intensity, of the band-edge emission of SnO₂/ZnS nanocomposites at 325 nm decreases progressively and rapidly with the increase of $R_{\text{Sn/Zn}}$, indicating that fast electron transfer takes place from photoexcited ZnS nanorods to SnO₂ QDs. Thus, the higher photocatalytic degradation efficiencies of SnO₂/ZnS nanocomposites are considered to result mainly from the increased separation rates of photogenerated charges. The photostability of SnO₂/ZnS nanocomposites is also improved due to the protection and charge-separation effects of decorating SnO₂ QDs. Our prepared SnO₂/ZnS nanocomposites are suggested to have great potential for photodegradation nanocatalysts in the field of waste-water treatment.

© 2016 Elsevier B.V. All rights reserved.

1. Introduction

Environmental pollution and energy shortage have emerged as serious problems with the development of technology and industry. Particularly, toxic and colored organic pollutants generated in textile and dye industry have significant negative effects on the nature of water, decreasing available clean water and destroying the ecosystem. Thus, the development of diverse advanced oxidation processes (AOPs) has been progressed by oxidation with radical species for environmental decontamination [1]. Among these AOPs, photocatalytic techniques based on semiconductors as green and efficient ways have great potential in conquering current energy and environmental issues using the inexhaustible solar

energy [2–5]. In addition, the techniques do not produce toxic by-products during photocatalytic processes.

It has been reported that metal sulfide nanostructures as photocatalysts can degrade various organic pollutants efficiently under light irradiation owing to their suitable catalytic function and band gap [6–10]. In particular, ZnS nanomaterials having a wide and direct band gap (3.80 eV for hexagonal wurtzite) are promising photocatalysts because of not only the rapid generation of electron-hole pairs by photo-excitation but also the highly negative reduction potential of their conduction band [11–14]. However, there are some serious drawbacks hindering their photocatalytic activity and practical applications, such as the rapid recombination of charge carriers and the absorption of limited UV light. Even the low separation efficiency of electron-hole pairs often causes photocorrosion problems, making ZnS very unstable and poorly recyclable as a photocatalyst [15–21]. Thus, in order to overcome these disadvantages, diverse strategies have been established such as the fabrication of porous and hollow structures, doping with nonmetals, and coupling with other noble metals and/or

* Corresponding author.

E-mail address: djjang@snu.ac.kr (D.-J. Jang).

¹ These authors contributed equally.

semiconductors [11–21]. One of the most extensively employed approaches is to combine a semiconductor with another semiconductor having different electron affinity and ionization potential [20–25]. In other words, the combination of two semiconductors having different redox potential levels provides a significant key role to attain charge separation effectively at interfacials, to extend the photoresponse range largely, and to prolong the lifetime of charge carriers considerably [23–31].

Heterojunction nanocomposites, where one semiconductor is partially coated by the other semiconductor, have received extraordinary attention as photocatalysis systems because both electrons and holes can readily participate in the redox reaction on their surfaces [25–31]. Furthermore, one-dimensional (1D) nanostructures as photocatalyst substrates have been extensively used due to their unique structural and electronic properties and superior performances in the heterojunction systems [23,27–29]. 1D nanostructures such as nanorods and nanowires/nanobelts possess several advantages as follows: large aspect ratios which can increase the capacity of light absorption; great separation efficiencies of photo-generated charge carriers due to their high mobility and straight transport pathways [31–34].

Tin oxide (SnO_2) having an n-type wide band gap (3.60 eV for tetragonal rutile) has been also well-known as a popular photocatalyst because of its high photocatalytic activity and stability, non toxicity, low cost, and ubiquitous availability [27,28,35–40]. Especially, its combination with ZnS nanomaterials can form excellent heterojunction photocatalysts having type II band offsets [36,37]. However, the conduction band (CB) of SnO_2 is more positive than the reduction potential of $\text{O}_2/\cdot\text{O}_2\text{H}$ (−0.05 eV vs NHE at pH 0) [30,31]. Thus, although the deposition of SnO_2 nanoparticles on ZnS nanomaterials provides an enhanced charge-separation efficiency, it cannot produce strong oxidizing species such as $\cdot\text{O}_2\text{H}$ to decompose water contaminants [30,31,40]. In contrast, the band gap of SnO_2 quantum dots (QDs) gets expanded gradually owing to the quantum confinement effect, as their sizes decrease. With the increase of the band gap, the CB of SnO_2 QDS shifts to the more negative potential, reducing O_2 to generate peroxy radicals ($\cdot\text{O}_2\text{H}$) [30,41–43].

In this work, we have fabricated SnO_2/ZnS nanocomposites of SnO_2 QDs-deposited ZnS nanorods as 1D heterojunction nanostructures through a facile two-step hydrazine-assisted hydrothermal process without using any complex surface treatments to introduce new functional molecules or additional inter-connectivity [42–44]. It is noteworthy that a rational synthesis of high-quality SnO_2/ZnS heterojunction nanocomposites via a simple and friendly manner has not been reported yet [36,37]. The photocatalytic activity and photostability of SnO_2/ZnS heterojunction nanostructures are much higher than the respective ones of ZnS nanorods. The decay time, as well as the intensity, of the band-edge emission of SnO_2/ZnS nanocomposites decreases progressively and rapidly with the increase of the SnO_2 content, indicating that the higher photocatalytic degradation efficiencies of SnO_2/ZnS nanocomposites result mainly from the increased separation rates of photogenerated charges. Our prepared SnO_2/ZnS nanocomposites are considered to have great potential for photodegradation nanocatalysts in the field of waste-water treatment.

2. Experimental section

2.1. Materials

Chemicals were used as received without further purification: $\text{N}_2\text{H}_4\cdot\text{H}_2\text{O}$ (l, 98%), ethylenediamine (l, 99%), and p-benzoquinone (BQ, s, >98%) from Alfa Aesar; ZnS (s, 99.99%), SnO_2 (s, <100 nm avg. part. size), ethylene diaminetetraacetic acid (EDTA, s, 99%),

telephthalic acid (TA, s, 98%), ZnCl_2 (s, >98%), and $\text{SnCl}_4\cdot 5\text{H}_2\text{O}$ (s, 98%) from Sigma-Aldrich; isopropyl alcohol (IPA, l, >99.5%), NaOH (s, >97%), sulfur (s, >99.0%), and ethanol (l, >99.0%) from Daejung Chemicals; rhodamine B (RhB, s) from Wako Pure Chemical. Ultra-pure deionized water (>17 M Ω cm) from Millipore Milli-Q System was used throughout the experiments.

2.2. Fabrication

SnO_2/ZnS heterojunction nanostructures of SnO_2 -deposited ZnS nanorods having a specific molar ratio of Sn/Zn were prepared using a simple two-step hydrazine-assisted hydrothermal method. In typical preparation of single-crystalline wurtzite ZnS nanorods [44], 7.5 mL of water, 7.5 mL of ethylenediamine, 15 mL of $\text{N}_2\text{H}_4\cdot\text{H}_2\text{O}$, 2.0 mmol of ZnCl_2 , and 2.0 mmol of sulfur were stirred vigorously for 30 min. The mixture solution was then loaded into a Teflon-lined stainless-steel autoclave with a capacity of 50 mL. The sealed autoclave was put into an oven at 180 °C for 9 h and cooled to room temperature (first step). 0.08, 0.16, 0.20, 0.24, or 0.30 mmol of $\text{SnCl}_4\cdot 5\text{H}_2\text{O}$ (s) was added into the 30 mL of the mixture solution containing 195 mg ZnS nanorods and stirred for 10 min vigorously. Then, the mixture solution was poured into the autoclave. Note that $R_{\text{Sn/Zn}}$, the molar ratio of Sn to Zn in the final mixture, was varied from 0.00 to 0.15. The sealed autoclave was put again into an oven preheated at 180 °C for another 6 h (second step). The resultant products were repeatedly centrifuged, washed with water several times, and finally dried in a vacuum at 60 °C for 5 h to obtain SnO_2/ZnS heterojunction nanostructures. The overall percent yield of produced SnO_2/ZnS ($R_{\text{Sn/Zn}} = 0.10$) nanocomposites was 96%.

2.3. Characterization

Transmission electron microscopy (TEM) images were obtained with a Hitachi H-7600 microscope while scanning electron microscopy (SEM) images were recorded with a MERLIN Compact microscope. While high-resolution X-ray diffraction (HRXRD) patterns were taken with a Bruker D8 DISCOVER diffractometer using $\text{Cu K}\alpha$ radiation (0.15418 nm), high-angle annular dark-field (HADDF) images and energy-dispersive X-ray (EDX) elemental mappings were measured utilizing a JEOL JEM-2100F scanning TEM (STEM) microscope. High-resolution TEM (HRTEM) images and selected area electron diffraction (SAED) patterns were recorded with a Tecnai F20 microscope. X-ray photoelectron spectroscopy (XPS) spectra were obtained by employing a KRATOS AXIS-HSi spectrometer having a 150 W Mg anode with a scan step of 0.1 eV, and observed binding energies were calibrated with the C 1s peak at 284.5 eV of contaminated carbon. UV–vis diffuse reflectance spectra were recorded using a StellaNet US/EPP 2000C spectrometer, and N_2 adsorption–desorption measurements were carried out using a Nova 2200e Quantachrome instrument. PL spectra were taken using an Ocean Optics USB2000+ detector with excitation of 266 nm pulses having a duration time of 6 ns from a Q-switched Quantel Brilliant Nd:YAG laser. To obtain PL decay kinetic profiles, 266 nm pulses from a mode-locked Quantel Pizzicato Nd:YAG laser of 25 ps were utilized for excitation, and a Hamamatsu C2830 streak camera of 10 ps attached with a Princeton Instruments RTE128H CCD detector was employed for detection. PL wavelengths were selected by combining cut-off and band-pass filters. To detect the generation of $\cdot\text{O}_2^-$ radical species, electron spin resonance (ESR) measurements were carried out using a Bruker EMX-plus X-band CW electron paramagnetic resonance spectrometer with spin-trap reagent 5,5-dimethyl-1-pyrroline N-oxide (DMPO, s, purchased from Sigma-Aldrich). Total organic carbon (TOC) was estimated using a Sievers 5310C TOC analyzer.

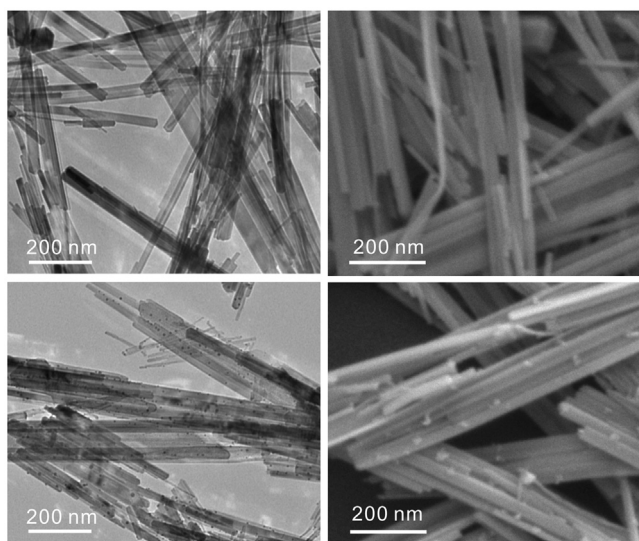


Fig. 1. TEM (left) and SEM (right) images of ZnS nanorods (top) and SnO₂/ZnS ($R_{\text{Sn/Zn}} = 0.10$) nanocomposites (bottom).

2.4. Photocatalysis

The photocatalytic performances of as-prepared SnO₂/ZnS nanocomposites as nanocatalysts were evaluated by monitoring the photodegradation reaction of RhB under ambient conditions. In a typical procedure, 30 mL of an aqueous suspension containing 5.0 mg nanocatalysts and 10 μM RhB was stirred for 1 h in the dark to assure the establishment of an adsorption-desorption equilibrium of RhB on the surfaces of nanocatalysts. The entire mixture solution was covered by the light beam of a 300 W Schoeffel LPS 255 HR xenon lamp. The mixture was stirred magnetically during irradiation, and an aliquot was taken at every 10 min and centrifuged (10000 rpm, 10 min) to separate the supernatant. The concentration of remnant RhB in the aliquots was monitored by measuring UV/vis absorption spectra with a Scinco S-3100 spectrometer. The photocatalytic activity was also investigated by measuring the photodegradation of phenol; the experimental procedure was the same except that 5 mg nanocatalysts and 10 μM RhB were replaced by 20 mg nanocatalysts and 0.43 mM phenol (s, 99+%, purchased from Alfa Aesar). Hydroxyl radicals formed on the surface of SnO₂/ZnS nanocomposites was detected by the PL technique using TA as the probing molecule [11,29]. Typically, 0.5 mg of a photocatalyst was added into 30 mL of a mixture solution containing 0.5 mM TA and 2 mM NaOH in a quartz reactor. The experimental procedure was similar to that for the measurement of photocatalytic efficiencies except that the RhB mixture solution was replaced by TA and NaOH. The PL spectra of 2-hydroxyterephthalic acid (TAOH) produced via a reaction with $\cdot\text{OH}$ were measured using a JASCO FP-8300 fluorescence spectrometer with excitation at 315 nm. In order to examine the reusability of the nanocatalysts, all the experimental parameters were kept constant. After each reaction, the color of an aqueous solution containing a nanocatalyst and RhB became colorless. Then, a fresh RhB solution has added into the resultant solution, where the initial concentration of RhB was always 10 μM . The experiments were repeated for 4 times under the same conditions.

3. Results and discussion

In order to examine the morphology and the structure of ZnS nanorods and SnO₂/ZnS nanocomposites, SEM and TEM images have been measured (Fig. 1). As-obtained ZnS nanorods have 1D morphology with a typical length of 1.8 μm and an average width

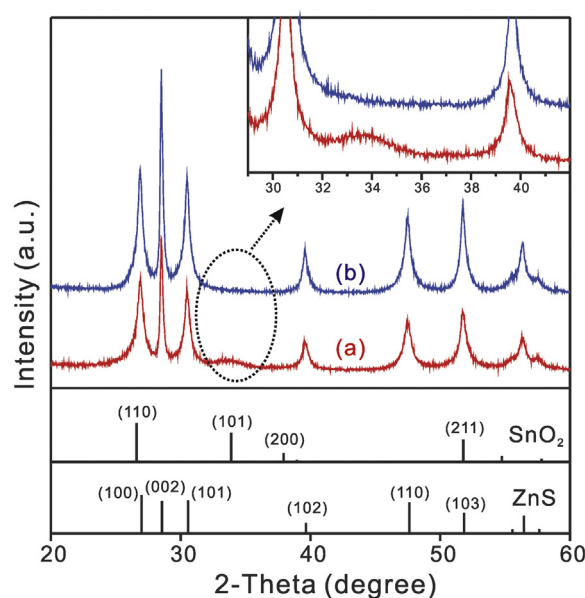


Fig. 2. HRXRD patterns of SnO₂/ZnS ($R_{\text{Sn/Zn}} = 0.10$) nanocomposites (a) and pristine ZnS nanorods (b). The standard diffraction lines of rutile SnO₂ and wurtzite ZnS are also shown for comparison.

of 90 nm while SnO₂ QDs having an average diameter of 3.0 nm are well dispersed on the surface of ZnS nanorods. Compared with the common base of NH₃ or NaOH, our employed base of hydrazine plays an important role in forming hybrid complexes [43]. Briefly, since the tin precursor of SnCl₄·5H₂O was added into the reaction mixture containing hydrazine, SnO₂ QDs of 3.0 nm have been produced via forming (SnCl₄)_m(N₂H₄)_n complexes [42,43]. The deposition of SnO₂ QDs on ZnS nanorods has been attributed to the decreasing force of the surface free energy between ZnS nanorods and SnO₂ QDs due to the high surface energy of SnO₂ QDs resulting from their small sizes [30,31,34]. Furthermore, the hydrothermal process also plays a key role in the deposition of SnO₂ QDs onto the surface of ZnS nanorods because collision and contact between ZnS nanorods and SnO₂ QDs, promoted by high temperature and pressure, are favorable to the binding of ZnS nanorods with SnO₂ QDs [19,25–28,34,42]. Because of direct and enhanced electron transfer resulting from close contact between ZnS and SnO₂ without having linker molecules, SnO₂/ZnS heterojunction nanocomposites have highly enhanced catalytic performances compared to pristine ZnS nanorods (see below) [19]. Fig. S1 also presents the TEM images of SnO₂/ZnS heterojunction nanocomposites having different $R_{\text{Sn/Zn}}$ values. As the value of $R_{\text{Sn/Zn}}$ was increased from 0.04 up to 0.15, the surface of ZnS nanorods has been found to be more densely covered with SnO₂ QDs, suggesting the loading and the size of SnO₂ QDs can be controlled by tuning the concentration of the tin precursor (Fig. S1a–d).

The crystal structure, phase purity, and average crystallite size of as-prepared samples have been investigated by monitoring HRXRD (Fig. 2). All the HRXRD patterns of SnO₂/ZnS samples exhibit standard diffraction peaks corresponding to hexagonal ZnS (JCPDS card no. 36-1450) or rutile SnO₂ (JCPDS card no. 41-1445); neither impurity peaks nor remarkable shifts from the diffraction peaks of pristine ZnS nanorods have been detected, suggesting that ZnS and SnO₂ exist together while no solid solution has been formed and the expansion or shrinkage of the ZnS lattice has not been observed in the nanocomposites (Fig. 2) [27,45,46]. Furthermore, the inset in Fig. 2 presents that the weak and broad diffraction peak of rutile SnO₂ QDs at 33° describes small grain sizes in the nanocomposites, and that SnO₂ QDs have been loaded well on the surface of ZnS nanorods [28–31]. The average crystallite sizes of ZnS and

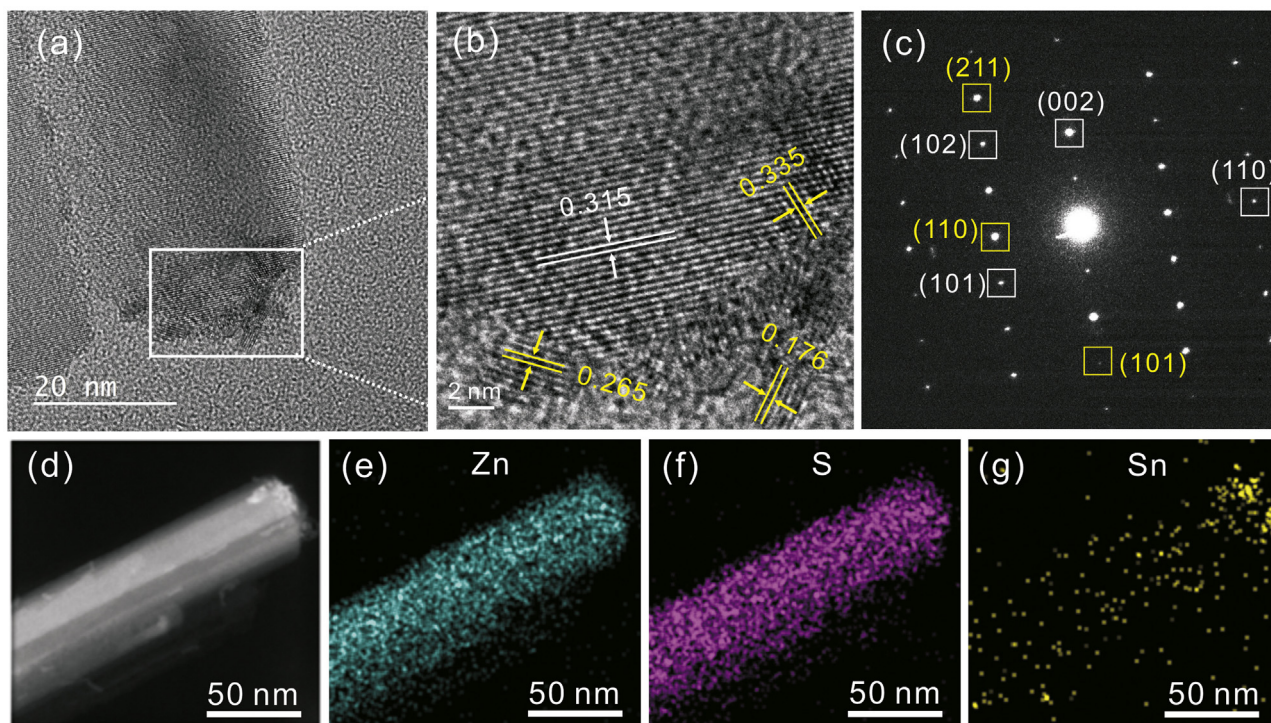


Fig. 3. HRTEM images (a and b) and SAED pattern (c), HAADF-STEM image (d), and EDX elemental mapping images (e–g) of a SnO_2/ZnS ($R_{\text{Sn/Zn}} = 0.10$) nanocomposite.

SnO_2 in the nanocomposites have been estimated from the peak widths of the (001) planes of hexagonal ZnS and the (101) planes of rutile SnO_2 , respectively, using the Scherrer equation [42,44], and the values have been listed in Table S1. As shown in Fig. S2, there is no obvious differences between SnO_2/ZnS ($R_{\text{Sn/Zn}} = 0.04$) nanocomposites and pristine ZnS nanorods, implying that rutile SnO_2 peaks have not been detected due to the low content of SnO_2 QDs [30,31,36]. When the molar ratio of Sn/Zn has increased from 0.08 to 0.15 gradually, the diffraction intensity of the rutile SnO_2 (101) planes at 33° , as well as the average crystallite size of SnO_2 QDs, has steadily enlarged while the intensities of the ZnS diffraction peaks have reduced due to the hinderance of SnO_2 QDs on the X-ray transmission [30,31]. It is noteworthy that the diffraction peaks of ZnS nanocrystals in the nanocomposites are still very sharp in spite of the decrement of the intensities, suggesting that the crystallinity of ZnS nanomaterials remains truly high even after loading SnO_2 QDs onto ZnS nanorods. Table S1 further shows that the chemical composition of all the samples has been analyzed by the EDX technique, revealing that Zn, S, Sn, and O elements exist together. In particular, the calculated actual molar ratios of Sn to Zn in Table S1 are consistent approximately with the respective $R_{\text{Sn/Zn}}$ values of SnO_2/ZnS nanocomposites, suggesting that the tin precursor added in the reaction mixture containing ZnS nanorods has been transformed almost entirely into SnO_2 QDs decorated on ZnS nanorods [25,31].

The HRTEM images of Fig. 3a and b reveal that the observed lattice spacings of SnO_2/ZnS ($R_{\text{Sn/Zn}} = 0.10$) heterojunction nanostructures are 0.315 and 0.335 nm which arise from the (001) planes of hexagonal ZnS and the (110) planes of rutile SnO_2 , respectively. Meanwhile, the other observed lattice spacings of 0.265 and 0.176 nm in Fig. 3b are attributed to the (101) and (211) planes of rutile SnO_2 , respectively. Thus, the HRTEM images of Fig. 3a and b designate that SnO_2 QDs have been deposited onto the surfaces of ZnS nanorods via interfacial junction without having any linker molecules. The SAED pattern of the SnO_2/ZnS ($R_{\text{Sn/Zn}} = 0.10$) nanocomposites supports that heterojunction nanostructures have

been well fabricated via a two-step hydrazine-assisted hydrothermal process (Fig. 3c) [25]. To understand the constitution and chemical composition of the heterojunction structures further, elemental analysis has been performed with the HAADF-STEM mode of EDX; SnO_2 QDs look brighter than the ZnS nanorod in the HAADF-STEM image of Fig. 3d because the atomic number of Sn (50) is larger than that of Zn (30). The EDX elemental mapping images of Fig. 3e–g also suggest that SnO_2 QDs are well distributed homogeneously on the surface of a ZnS nanorod. In the case of pristine ZnS nanorods (Fig. S3), their morphology, structure, and composition have remained invariant regardless of a subsequent hydrothermal process, and all of the lattice fringes arrange along the same direction of the (001) planes. These are also supported by the SAED pattern and the EDX mapping images of Fig. 3. Finally, based on the above results, it can be concluded that as the morphology of SnO_2/ZnS nanocomposites resembles that of ZnS nanorods, SnO_2 QDs are homogeneously distributed on ZnS nanorods. This may be beneficial for the rapid interfacial transfer of photogenerated charge carriers from ZnS nanorods to SnO_2 QDs in photocatalysis (see below) [21,29–31].

Fig. 4 shows that XPS has been employed to investigate the surface chemical states of obtained SnO_2/ZnS ($R_{\text{Sn/Zn}} = 0.10$) nanocomposites. The binding energies (BEs) of $\text{Zn } 2p_{3/2}$ and $\text{Zn } 2p_{1/2}$ were observed as 1044.23 and 1021.03 eV, respectively (Fig. 4a), while the BEs of $\text{S } 2p_{3/2}$ and $\text{S } 2p_{1/2}$ were measured as 160.83 and 162.03 eV, respectively (Fig. 4b) [12,19,44]. Compared with the Zn and S XPS spectra of pristine ZnS nanorods (Fig. S4a and b), the respective spectra of nanocomposites have been hardly changed in spite of the incorporation of SnO_2 QDs, demonstrating that the structure of ZnS nanorods in SnO_2/ZnS nanocomposites are almost the same as that in pristine ZnS nanorods [27]. Two sharp peaks at 486.15 and 494.48 eV in Fig. 4c have been assigned to $\text{Sn } 3d_{5/2}$ and $\text{Sn } 3d_{3/2}$, respectively [31]. The spin-orbit separation of 8.3 eV between two peaks in Fig. 4c confirms that the oxidation state of Sn atoms adsorbed on the surface of the nanocomposites is +4 [31,38]. The O 1s XPS spectrum of Fig. 4d has been

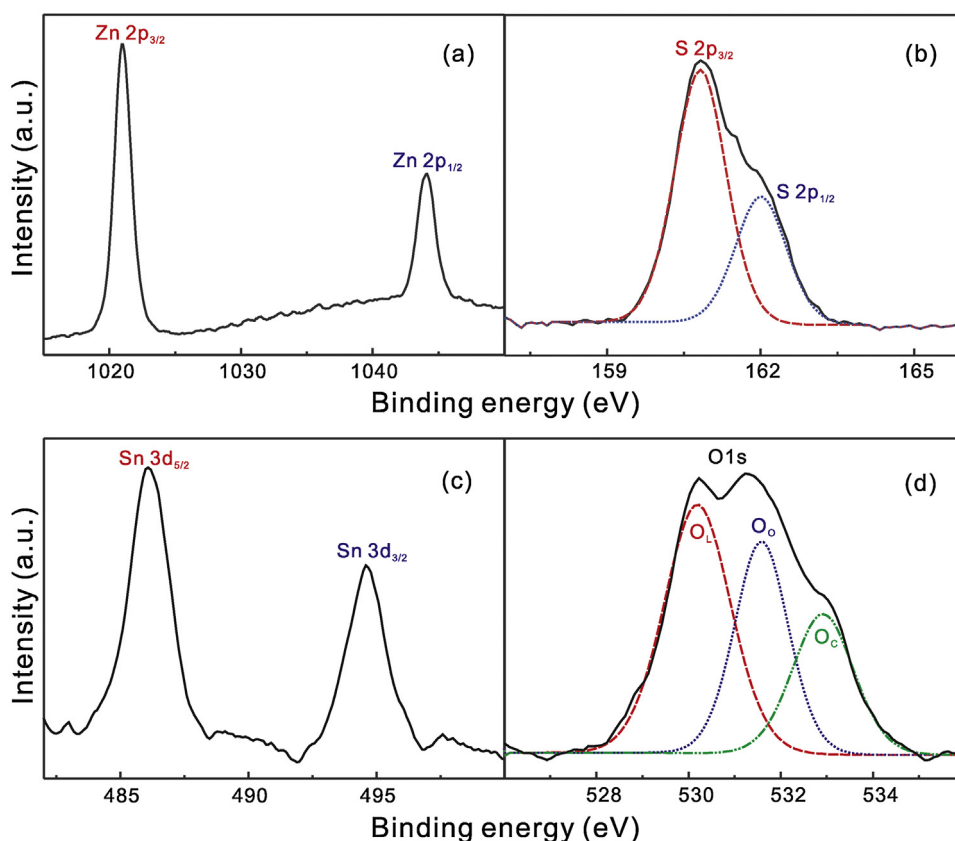


Fig. 4. Zn 2p (a), S 2p (b), Sn 3d (c), and O 1s (d) XPS spectra of SnO₂/ZnS ($R_{\text{Sn/Zn}} = 0.10$) nanocomposites. The O 1s spectrum has been deconvoluted into three Gaussian curves.

deconvoluted into three peaks; the O_L peak at 530.19 eV is associated with the lattice oxygen of SnO₂ QDs, the O_O peak at 531.58 eV is attributed to chemisorbed oxygen, and the O_C peak at 532.92 eV is ascribed to chemically adsorbed hydroxyl groups [27,31,40,50]. Fig. S4c shows that the BE values of the O_O and O_C peaks for ZnS nanorods are 531.16 and 532.52 eV [47,48]. The BE values of the O_O and O_C peaks have increased by 0.42 and 0.40 eV, respectively, with the incorporation of SnO₂ QDs because the electronegativity value of Sn (1.88) is higher than that of Zn (1.65). Furthermore, Fig. S4c indicates that any peak around 530 eV, attributable to the BE of the O_L peak in ZnO [48–50], has not been observed at all for pristine ZnS nanorods. This implies that the oxidation of ZnS has not been taken place at all to form ZnO during the two-step hydrothermal process. Thus, together with the presented HRXRD and HRTEM results, the XPS results demonstrate that SnO₂/ZnS nanocomposites of SnO₂ QDs-decorated ZnS nanostructures have been well prepared via the two-step hydrazine-assisted hydrothermal process.

The UV–vis diffuse-reflectance spectra of SnO₂/ZnS nanocomposites having specifically varied Sn/Zn molar ratios have been investigated (Fig. 5). Pristine ZnS nanorods have limited UV photoresponse below 340 nm (3.7 eV) while SnO₂/ZnS nanocomposites have extended visible absorption up to 500 nm due to the newly generated interface energy states between ZnS and SnO₂ in the heterojunction structures [23–25,51]. Indeed, as shown in Fig. S5, a new absorption band appears at 350–500 nm for SnO₂/ZnS nanocomposites, and it has been attributed to the new interfacial states whose energy levels are localized within the band gap of ZnS, reducing the band gap energy of the nanocomposites compared with that of pristine ZnS nanorods [23,51]. In this regard, we consider that the narrowed band gap can make the interfaces generate charge carriers under the visible light (see below). Fig. 5 also indicates that light absorption in the visible range increases

with the increment of SnO₂ contents in the heterojunction nanostructures. Fig. S6a–c surely shows that SnO₂/ZnS nanocomposites degrade RhB indeed under visible light irradiation ($\lambda \geq 400$ nm), whereas pristine ZnS nanorods hardly degrade RhB under the same conditions. Thus, we can conclude that extended photoresponse up to 500 nm is also an important factor to enhance the photocatalytic performances of SnO₂/ZnS nanocomposites.

The photocatalytic properties of SnO₂/ZnS nanocomposites having specifically varied molar ratios of Sn/Zn have been evaluated by observing the time-dependent absorbance changes of RhB under light irradiation. The photocatalytic performances of commercial ZnS were also investigated in the same conditions for comparison. As presented in Fig. S7a–f, the characteristic absorption of RhB at 554 nm diminishes gradually with the increase of the light

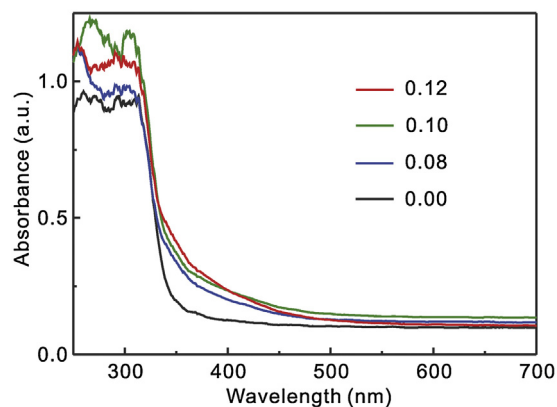


Fig. 5. UV–vis diffuse-reflectance spectra of SnO₂/ZnS nanocomposites with indicated $R_{\text{Sn/Zn}}$ values.

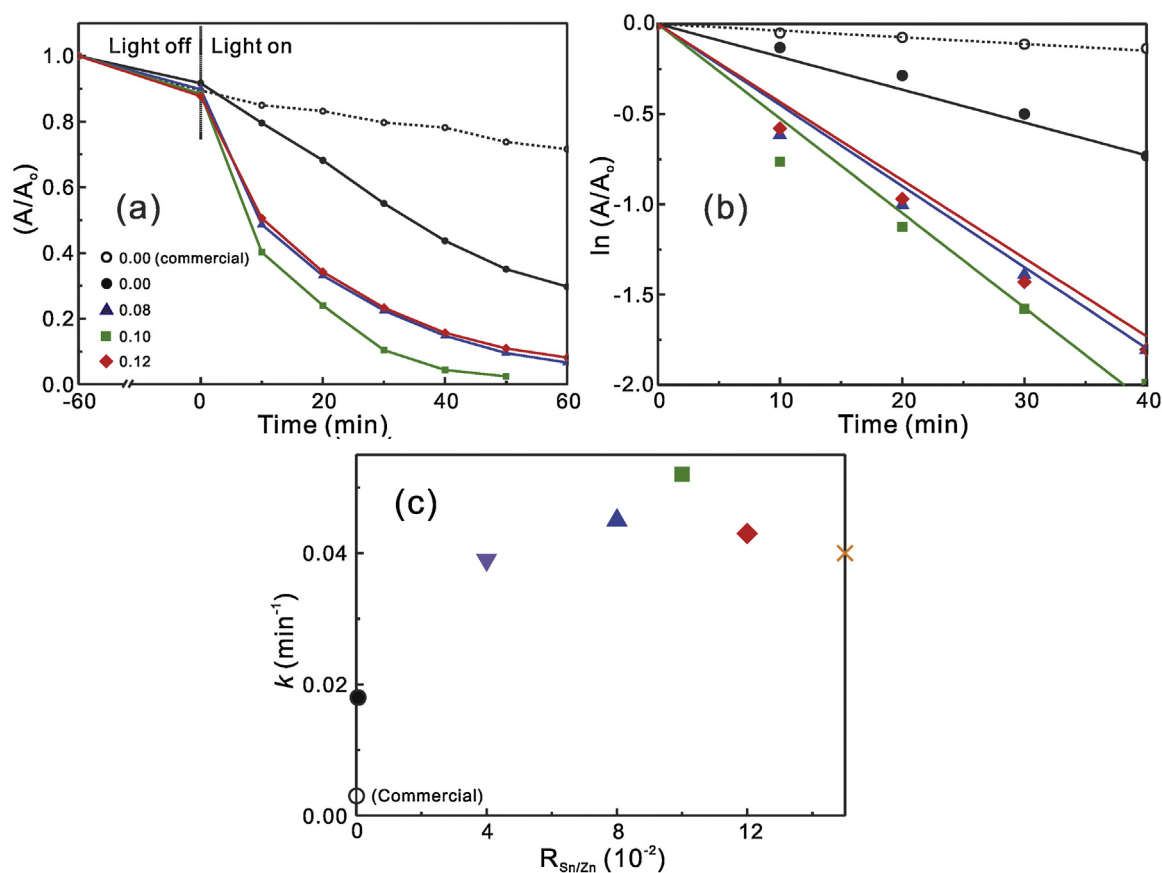


Fig. 6. Decay kinetic profiles at 554 nm (a), first-order decay profiles (b) and degradation rate constants (c) of RhB via SnO₂/ZnS nanocomposites with indicated R_{Sn/Zn} values.

irradiation time [52]. Additionally, a concomitant blue shift in the absorption maximum has been observed together, implying that the photodegradation of RhB goes through two competitive processes; one is the destruction of the conjugated chromophore structure, which bring about absorption loss at 554 nm [53], and the other is the stepwise N-deethylation reaction that removes the N-ethyl groups sequentially from the RhB molecules [6,52]. RhB has been rarely degraded either without catalysts or with commercial ZnS, whereas it has been rapidly and completely degraded in the presence of SnO₂/ZnS nanocomposites. In particular, through the sequential remediation of heterojunction components, the photocatalytic efficiency of SnO₂/ZnS (R_{Sn/Zn} = 0.10) nanocomposites has been found to be significantly higher than that of any other studied nanocatalysts; the efficiency of SnO₂/ZnS (R_{Sn/Zn} = 0.10) nanocomposites is 3 times higher than that of pristine ZnS nanorods and 17 times higher than that of commercial ZnS. The pseudo-first order photodegradation kinetic profiles of RhB have been exploited (Fig. 6a) to obtain the kinetic constants of Table 1 using $\ln(A/A_0) = -kt$, where k is the rate constant and t is the time [53]. In

addition, the photodegradation kinetic data of phenol in Fig. S8 also demonstrate that the photocatalytic activity of SnO₂/ZnS having R_{Sn/Zn} = 0.10 ($k = 0.0074 \text{ min}^{-1}$) is much higher than that of pristine ZnS ($k = 0.0028 \text{ min}^{-1}$). These results are almost consistent with the photodegradation kinetic data of RhB. Fig. 6b and Fig. S8 indicate that the photocatalytic performances of SnO₂/ZnS hybrid nanostructures are enhanced gradually with the increase of R_{Sn/Zn} until the value becomes 0.1. However, as R_{Sn/Zn} increases over 0.1, the photocatalytic efficiency of SnO₂/ZnS nanocomposites rather decreases. Thus, excess SnO₂ QDs on the surface of ZnS nanorods are considered to act as the recombination sites, rather than the separation sites, of photogenerated charges [19,25–27]; excessive SnO₂ shells not only block the transmission of light into ZnS nanorods but also diminish the accessibility of RhB molecules to the active sites of ZnS nanorods surfaces, hardly increasing the generation of charge carriers from ZnS nanorods [26,27,30,31,49].

N₂ adsorption-desorption isotherms of as-prepared SnO₂/ZnS nanocomposites with different molar ratios of Sn/Zn have been evaluated to characterize the surface area and the porosity of

Table 1
Catalytic degradation rate constants, BET surfaces areas, and average pore sizes of nanocatalysts.

Nanocatalyst	R _{Sn/Zn}	k (min ⁻¹)	BET surface area (m ² /g)	Average pore size (nm)
No catalysts	–	0.001		
Commercial SnO ₂	∞	0.020		
Commercial ZnS	0.00	0.003		
ZnS nanorods	0.00	0.018	76.0	63.7
Nanocomposites	0.04	0.039	83.3	32.5
Nanocomposites	0.08	0.045	95.2	29.9
Nanocomposites	0.10	0.052	97.1	29.7
Nanocomposites	0.12	0.043	98.8	30.9
Nanocomposites	0.15	0.040	99.8	30.9

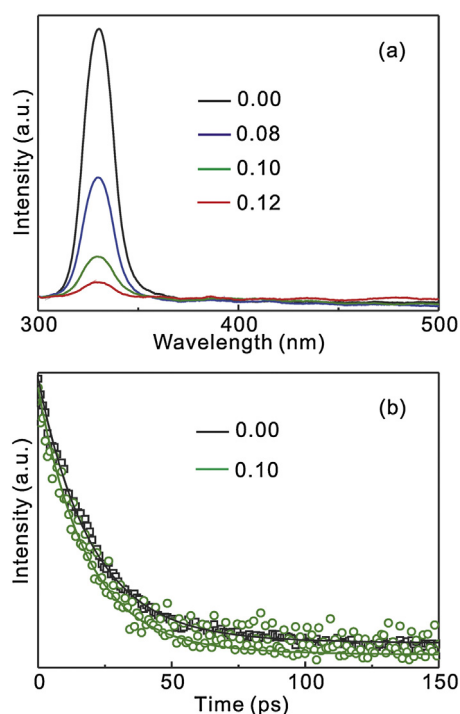


Fig. 7. PL spectra (a) and emission decay profiles at 325 ± 20 nm (b) of SnO₂/ZnS nanocomposites with indicated $R_{\text{Sn/Zn}}$ values. Samples were suspended in ethanol and excited with 266 nm laser pulses.

each nanocatalyst (Fig. S9). We have found out that our samples exhibit type-IV isotherms including typical type-H3 hysteresis loops (at $P/P_0 > 0.8$) according to the IUPAC classification, implying the formation of large mesopores and macropores [18,21,26,31]. The Brunauer-Emmett-Teller (BET) surface areas and pore sizes of SnO₂/ZnS nanocomposites with diverse $R_{\text{Sn/Zn}}$ values have been summarized in Table 1. The surface area of the nanocomposites gradually increases with the increase of the SnO₂ content until the molar ratio of Sn/Zn becomes 0.1, and the enhanced surface area is suggested to offer the higher adsorption ability of the catalyst surface toward organic molecules and the higher generation ability of charge carriers from active sites [54]. Thus, these results support as well that heterojunction nanocomposites have higher photocatalytic ability than single-component photocatalysts do partly due to the increased surface area. However, when the molar ratio of Sn/Zn increases over 0.1, the surface area of nanocomposites has remained almost constant and the photocatalytic efficiency of nanocomposites has decreased slightly due to a few reasons mentioned above. Overall, we consider that the increased surface area is not the only factor responsible for determining the photocatalytic activity.

PL spectra have often been exploited to examine the separation, transfer, and recombination of photogenerated charge carriers [9,10,55–58]. To investigate the charge separation effect of SnO₂ QDs-deposited ZnS nanostructures, we have observed the PL spectra of SnO₂/ZnS nanocomposites having various values of $R_{\text{Sn/Zn}}$ (Fig. 7a). An intense PL peak at 325 nm arising from band-edge emission (BEE) has been discovered in pristine ZnS nanorods while defect-related emission in the visible region has not been monitored at all, demonstrating that the structure of ZnS nanorods is perfectly crystalline [44]. With the incorporation of SnO₂ QDs, the BEE of ZnS nanorods decreases drastically while no other PL peaks appear newly; the PL of SnO₂/ZnS nanocomposites decreases rapidly with the increase of $R_{\text{Sn/Zn}}$ [57,58]. The quenching phenomenon is mainly associated with the efficient charge-separation effect of the type II band configuration consisting of ZnS nanorods

Table 2

PL intensities and emission decay kinetic constants of SnO₂/ZnS nanocomposites with indicated $R_{\text{Sn/Zn}}$ values suspended in ethanol.

$R_{\text{Sn/Zn}}$	I_0^a	Decay time (ps)	τ_0^b (ps)	k_{ET} (10^9 s^{-1})
0.00	1.00	20 (94%) + 700 (6%) ^c	60.8	–
0.08	0.45	19 (95%) + 600 (5%)	48.1	4.3
0.10	0.15	18 (97%) + 100 (3%)	20.4	33
0.12	0.05	17 (98%) + 70 (2%)	18.1	39

^a Relative PL intensity.

^b Mean decay time.

^c Initial amplitude percentage of each component.

and SnO₂ QDs [9,10,55]. This result is also consistent with the enhanced photocatalytic activity of heterojunction nanocomposites in comparison with that of pristine ZnS nanorods. To probe electron transfer dynamics across the interface further, we have also measured the time-resolved PL decay times of SnO₂/ZnS nanocomposites having controlled $R_{\text{Sn/Zn}}$ values [9,10,56–58]. To the best of our knowledge, the decay kinetic study of BEE at 325 nm for ZnS nanoparticles has not been reported yet. Fig. 7b indicates that the BEE of SnO₂/ZnS ($R_{\text{Sn/Zn}} = 0.10$) nanocomposites decays much faster than that of pristine ZnS nanorods. Furthermore, Fig. S10 shows that the PL of SnO₂/ZnS nanocomposites decays rapidly and progressively with the increase of the $R_{\text{Sn/Zn}}$ value, suggesting that the decay time of SnO₂/ZnS nanocomposites is reduced because of electron transfer from photoexcited ZnS nanorods to SnO₂ QDs [56–58]. Each decay kinetic profile has been fitted biexponentially (Table 2); the fast decay component has been ascribed to the intrinsic recombination of electrons and holes in exciton states while the slow decay component has been considered to arise from the radiative decay of charge carriers in surface states [8]. Whereas the fast component remains almost invariant, the slow component decreases sharply with the increase of the $R_{\text{Sn/Zn}}$ value. Thus, this suggests that the drastic PL decrease of SnO₂/ZnS nanocomposites in Fig. 7 with the increase of $R_{\text{Sn/Zn}}$ is due to enhanced electron transfer from the surface states of ZnS nanorods to SnO₂ QDs. The mean PL decay time (τ_0) of the nanocomposites also diminishes rapidly with the increase of $R_{\text{Sn/Zn}}$ (Table 2). The apparent rate constant of electron transfer (k_{ET}) from ZnS nanorods to SnO₂ QDs (Table 2) has been calculated as [9,10,56–58]

$$k_{\text{ET}} = [\tau_0(\text{SnO}_2/\text{ZnS})]^{-1} - [\tau_0(\text{ZnS})]^{-1} \quad (1)$$

Considering all the above results, we can deduce that the higher photocatalytic degradation efficiencies of SnO₂/ZnS nanocomposites result mainly from the enhanced separation rates of photogenerated charges in SnO₂/ZnS heterojunction nanostructures, which can be tuned by adjusting $R_{\text{Sn/Zn}}$ values.

The above presented results have shown that as-prepared SnO₂/ZnS heterojunction nanocomposites have excellent photocatalytic performances in the degradation of RhB. To elucidate the photodegradation mechanism of RhB clearly, we have investigated the main reactive species of h^+ , $\bullet\text{O}_2^-$, and $\bullet\text{OH}$ involved in the photocatalytic reaction [31,34]. Here, EDTA, BQ, and IPA were introduced to act as the scavengers of h^+ , $\bullet\text{O}_2^-$, and $\bullet\text{OH}$, respectively, in the photocatalytic process [59,60]. Fig. 8 displays the photocatalytic efficiencies of pristine ZnS nanorods and SnO₂/ZnS ($R_{\text{Sn/Zn}} = 0.10$) nanocomposites for the decomposition of RhB in the presence of different scavengers. While the addition of 30 μmol BQ ($\bullet\text{O}_2^-$ scavenger) or 1.0 mL IPA ($\bullet\text{OH}$ scavenger) into a reaction mixture solution drastically reduces the photodegradation efficiency of RhB, the addition of 30 μmol EDTA (h^+ scavenger) into a reaction mixture solution has little effect on the photocatalytic activity. These results demonstrate that $\bullet\text{O}_2^-$ and $\bullet\text{OH}$ are main reactive species to decompose RhB, whereas h^+ does not play an important role in the photodegradation reaction of RhB. To further examine the generation of $\bullet\text{OH}$ radicals involved in that reaction,

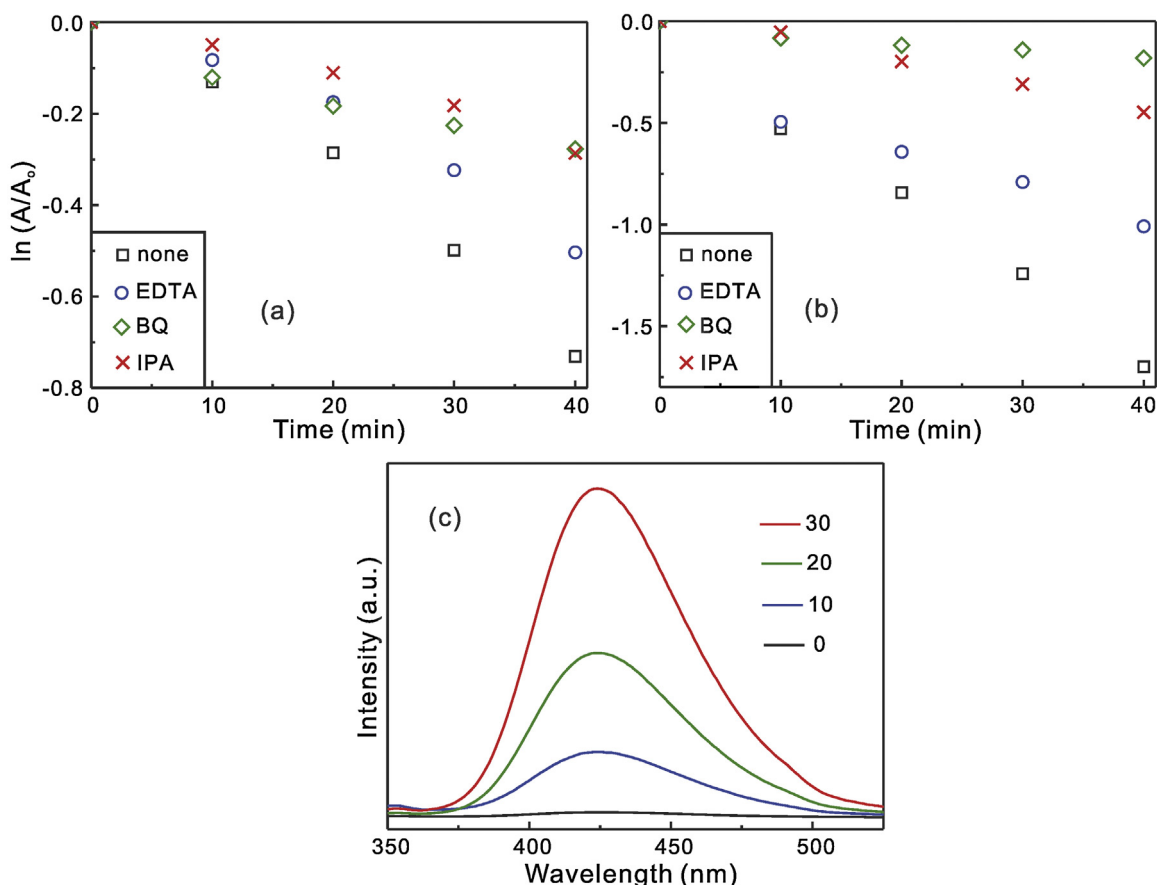


Fig. 8. First-order decay profiles of RhB via pristine ZnS (a) and SnO_2/ZnS ($R_{\text{Sn}/\text{Zn}} = 0.10$) nanocomposites (b) in the presence of indicated scavengers. PL spectra of TAOH generated by light irradiation in the presence of SnO_2/ZnS ($R_{\text{Sn}/\text{Zn}} = 0.10$) nanocomposites for durations indicated in the units of min (c).

$\cdot\text{OH}$ radicals have been detected by measuring PL spectra of TA as a probe molecule, which reacts with $\cdot\text{OH}$ to produce a fluorescent product, 2-hydroxyterephthalic acid (TAOH) [11,29]. The PL intensity of TAOH has tendency to increase proportionally with the amount of $\cdot\text{OH}$ generated on the surfaces of photocatalysts [59,60]. Fig. 8c indicates that the PL intensity has increased gradually with the increase of the irradiation time, manifesting that $\cdot\text{OH}$ is produced during the photocatalytic reaction. The ESR technique has also been used to detect the $\cdot\text{O}_2^-$ radical species evolved during the photocatalytic reaction process. 3 mL of an aqueous suspension containing 5.0 mg nanocatalysts and 50 mM DMPO, a well-known spin-trapping reagent, was irradiated with the xenon lamp for 1 h. As shown in Fig. S11, no ESR signals were observed in the dark condition whereas six characteristic peaks were monitored under light irradiation, revealing that the $\cdot\text{O}_2^-$ radicals were produced to play a key role in the photocatalytic reaction [58]. Overall, from the results of ESR and the PL spectra of TAOH, we have concluded that light irradiation was essential to the generation of $\cdot\text{O}_2^-$ and $\cdot\text{OH}$ radicals.

Based on the above results, the photodegradation mechanism of RhB over SnO_2/ZnS nanocomposites has been schematically illustrated in Fig. 9. Under light irradiation, charge carriers are generated on both ZnS nanorods and SnO_2 QDs, and charge transfers take place between two nanomaterials; photo-excited electrons on the CB of ZnS nanorods transfer to the CB of SnO_2 QDs while photo-generated holes in the valence band (VB) of SnO_2 migrate into the VB of ZnS through interfacial surfaces until their Fermi levels align [40,55–58]. Furthermore, an internal electrostatic field at the heterojunction interface facilitates the formation of charge-transfer states and depletion layers within the nanocomposites [27–31].

As a consequence, the recombination of electrons and holes in the nanocomposites is suppressed, giving more chances for electrons and holes to take part in redox reactions on the surfaces. Electrons are trapped by adsorbed O_2 to produce superoxide radicals ($\cdot\text{O}_2^-$), which is a strong oxidant capable of decomposing RhB effectively [27–31,59,60]. Meanwhile, simultaneously generated holes in ZnS can oxidize RhB molecules directly, which are bound to the surfaces of SnO_2/ZnS nanocomposites [59,60]. Moreover, if the adsorption of organic pollutants is insignificant, holes might also react with OH^- adsorbed on the surfaces of the photocatalysts to produce hydroxyl radicals ($\cdot\text{OH}$), which concurrently assist the decomposition of organic pollutants [11,12,47,60]. Hence, due to the synergistic effects of superoxide anion radicals, hydroxyl radicals and holes, SnO_2/ZnS heterojunction nanocomposites are suggested to have significantly enhanced catalytic performances for RhB photodegradation. Consequently, taking all the above facts into consideration, we assert that the extension of the photoreaction range to the visible region, the increment of the surface area, and the synergistic charge-separation effect of heterojunctions between ZnS and SnO_2 without having any linker molecules are responsible together for the highly enhanced photocatalytic activity of SnO_2/ZnS ($R_{\text{Sn}/\text{Zn}} = 0.10$) nanocomposites. Furthermore, in order to confirm the efficient mineralization of organic carbon during the photodegradation of RhB by SnO_2/ZnS ($R_{\text{Sn}/\text{Zn}} = 0.10$) nanocomposites, TOC measurements were conducted at scheduled intervals of light irradiation as shown in Fig. S12 [52]. The values of TOC have decreased gradually with the increase of the light irradiation time, demonstrating clearly that the mineralization of RhB occurs during its photocatalytic degradation by SnO_2/ZnS nanocomposites.

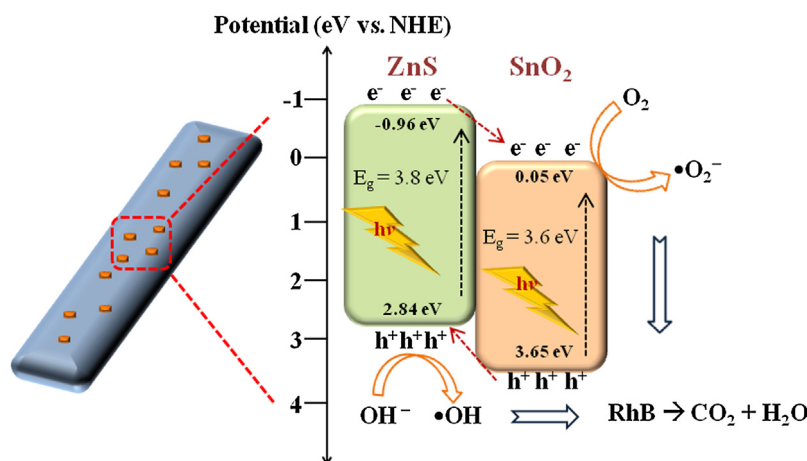


Fig. 9. Schematic for the degradation mechanism of RhB over a SnO_2/ZnS heterojunction nanostructure under light irradiation.

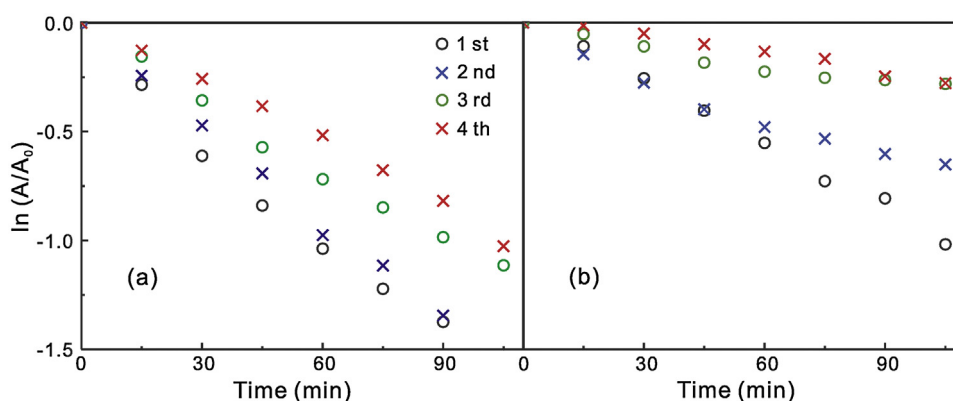


Fig. 10. Stability test of SnO_2/ZnS ($R_{\text{Sn/Zn}} = 0.10$) nanocomposites (a) and pristine ZnS nanorods (b) via repeated photocatalytic RhB-degradation experiments.

Although photostability during photocatalytic reactions is an important factor, it is well-known that metal sulfides have tendency to be unstable because of photocorrosion problems [6,11–19]. Thus, in order to check the stability of pristine ZnS nanorods and SnO_2/ZnS ($R_{\text{Sn/Zn}} = 0.10$) nanocomposites, recycling tests have been carried out (Fig. 10). From the second recycling test experiment, recycled SnO_2/ZnS ($R_{\text{Sn/Zn}} = 0.10$) nanocomposites revealed more enhanced stability, as well as higher catalytic activity, than recycled pristine ZnS nanorods, suggesting that decorated SnO_2 QDs enhance not only the photocatalytic activity but also the stability of ZnS nanorod [26,31,56–58]. We consider that the photostability of ZnS nanorods has been enhanced substantially because decorating SnO_2 QDs facilitate the separation of photogenerated charges extensively and they act as partial shells to inhibit photocorrosion taking place from the surface of ZnS. However, after three runs of RhB photodegradation, the photocatalytic activity of both samples has been somewhat reduced. Thus, we recognize that the loading of SnO_2 QDs cannot resolve the problems of ZnS photocorrosion completely [31].

4. Conclusions

SnO_2 QDs with a typical diameter of 3.0 nm have been deposited on the surfaces of ZnS nanorods having an average length of 1.8 μm and an average width of 90 nm via a facile two-step hydrazine-assisted hydrothermal method without involving any surface treatments to enhance photocatalytic activity and photostability. The photocatalytic activity of SnO_2/ZnS ($R_{\text{Sn/Zn}} = 0.10$)

nanocomposites is 3 times higher than that of pristine ZnS nanorods and 17 times higher than that of commercial ZnS. The incorporation of SnO_2 QDs increases the photocatalytic efficiency of ZnS nanorods based on the following reasons: photogenerated charge carriers are readily separated owing to type II band configuration and direct contact at interfaces without having any linker molecules; active surface sites are increased to adsorb more dye molecules; the light absorption range is extended to the visible region, generating more charge carriers on the surfaces of heterojunction structures. With the increase of $R_{\text{Sn/Zn}}$, the picosecond decay time, as well as the PL intensity, of the BEE of SnO_2/ZnS nanocomposites at 325 nm decreases progressively and rapidly, directly indicating that fast electron transfer takes place from photoexcited ZnS nanorods to SnO_2 QDs. Thus, we can suggest that the higher photocatalytic degradation efficiencies of SnO_2/ZnS nanocomposites result mainly from the enhanced separation rates of photogenerated charges in SnO_2/ZnS heterojunction nanostructures. Finally, compared with pristine ZnS nanorods, the photostability of SnO_2/ZnS nanostructures is also enhanced due to the protection and charge-separation effects of decorating SnO_2 QDs.

Acknowledgment

This work has been supported by the National Research Foundation of Korea (2015-051798).

Appendix A. Supplementary data

Supplementary data associated with this article can be found, in the online version, at <http://dx.doi.org/10.1016/j.apcatb.2016.12.063>.

References

- [1] P.V. Kamat, D. Meisel, *Curr. Opin. Colloid Interface Sci.* 7 (2002) 282–287.
- [2] R. Marschall, *Adv. Funct. Mater.* 24 (2014) 2421–2440.
- [3] H. Wang, L. Zhang, Z. Chen, J. Hu, S. Li, Z. Wang, J. Liu, X. Wang, *Chem. Soc. Rev.* 43 (2014) 5234–5244.
- [4] H.-B. Kim, H. Kim, W.I. Lee, D.-J. Jang, *J. Mater. Chem. A* 3 (2015) 9714–9721.
- [5] A. Kudo, Y. Miseki, *Chem. Soc. Rev.* 38 (2009) 253–278.
- [6] Y. Kim, H.-B. Kim, D.-J. Jang, *J. Mater. Chem. A* 2 (2014) 5791–5799.
- [7] K. Li, R. Chen, S.-L. Li, M. Han, S.-L. Xie, J.-C. Bao, Z.-H. Dai, Y.-Q. Lan, *Chem. Sci.* 6 (2015) 5263–5268.
- [8] H.-B. Kim, D.-J. Jang, *Nanoscale* 8 (2016) 403–410.
- [9] D. Wang, H. Zhao, N. Wu, M.A. El Khakani, D. Ma, *J. Phys. Chem. Lett.* 1 (2010) 1030–1035.
- [10] B.-R. Hyun, Y.-W. Zhong, A.C. Bartnik, L. Sun, H.D. Abruna, F.W. Wise, J.D. Goodreau, J.R. Matthews, T.M. Leslie, N.F. Borrelli, *ACS Nano* 2 (2008) 2206–2212.
- [11] X. Yu, J. Yu, B. Cheng, B. Huang, *Chem. Eur. J.* 15 (2009) 6731–6739.
- [12] G. Wang, B. Huang, Z. Li, Z. Lou, Z. Wang, Y. Dai, M.-H. Whangbo, *Sci. Rep.* 5 (2015) 8544.
- [13] J.S. Hu, L.L. Ren, Y.G. Guo, H.P. Liang, A.M. Cao, L.J. Wan, C.L. Bai, *Angew. Chem. Int. Ed.* 117 (2005) 1295–1299.
- [14] K. Chakraborty, S. Chakrabarty, P. Das, S. Ghosh, T. Pal, *Mater. Sci. Eng. B* 204 (2016) 8–14.
- [15] J. Zhang, L. Wang, X. Liu, X.a. Li, W. Huang, *J. Mater. Chem. A* 3 (2015) 535–541.
- [16] J. Zhang, Q. Zhang, L. Wang, W. Huang, *Sci. Rep.* 6 (2016) 27241.
- [17] J. Zhang, Q. Wang, L. Wang, X.a. Li, W. Huang, *Nanoscale* 7 (2015) 10391–10397.
- [18] Q. Li, H. Meng, P. Zhou, Y. Zheng, J. Wang, J. Yu, J. Gong, *ACS Catal.* 3 (2013) 882–889.
- [19] S. Ham, Y. Kim, M.J. Park, B.H. Hong, D.-J. Jang, *RSC Adv.* 6 (2016) 24115–24120.
- [20] X. Yang, H. Xue, J. Xu, X. Huang, J. Zhang, Y.-B. Tang, T.-W. Ng, H.-L. Kwong, X.-M. Meng, C.-S. Lee, *ACS Appl. Mater. Interfaces* 6 (2014) 9078–9084.
- [21] J. Zhang, J. Yu, Y. Zhang, Q. Li, J.R. Gong, *Nano Lett.* 11 (2011) 4774–4779.
- [22] P.-J. Wu, J.-W. Yu, H.-J. Chao, J.-Y. Chang, *Chem. Mater.* 26 (2014) 3485–3494.
- [23] M. Kwiatkowski, I. Bezverkhy, M. Skompska, *J. Mater. Chem. A* 3 (2015) 12748–12760.
- [24] J. Lahiri, M. Batzill, *J. Phys. Chem. C* 112 (2008) 4304–4307.
- [25] Z. Wang, S.-W. Cao, S.C.J. Loo, C. Xue, *CrystEngComm* 15 (2013) 5688–5693.
- [26] Y. Min, G. He, Q. Xu, Y. Chen, *J. Mater. Chem. A* 2 (2014) 2578–2584.
- [27] C. Wang, C. Shao, X. Zhang, Y. Liu, *Inorg. Chem.* 48 (2009) 7261–7268.
- [28] L. Zhu, M. Hong, G.W. Ho, *Sci. Rep.* 5 (2015) 11609.
- [29] S. Khanchandani, S. Kundu, A. Patra, A.K. Ganguli, *J. Phys. Chem. C* 116 (2012) 23653–23662.
- [30] K.-T. Lee, C.-H. Lin, S.-Y. Lu, *J. Phys. Chem. C* 118 (2014) 14457–14463.
- [31] Y. Liu, P. Zhang, B. Tian, J. Zhang, *ACS Appl. Mater. Interfaces* 7 (2015) 13849–13858.
- [32] Z.-J. Jiang, D.F. Kelley, *J. Phys. Chem. C* 115 (2011) 4594–4602.
- [33] Y. Kim, S.J. Kim, S.-P. Cho, B.H. Hong, D.-J. Jang, *Sci. Rep.* 5 (2015) 12345.
- [34] S. Liu, N. Zhang, Z.-R. Tang, Y.-J. Xu, *ACS Appl. Mater. Interfaces* 4 (2012) 6378–6385.
- [35] Y. Liu, Y. Jiao, Z. Zhang, F. Qu, A. Umar, X. Wu, *ACS Appl. Mater. Interfaces* 6 (2014) 2174–2184.
- [36] X. Meng, F. Wu, J. Li, *J. Phys. Chem. C* 115 (2011) 7225–7229.
- [37] X. Huang, Y.-Q. Yu, J. Xia, H. Fan, L. Wang, M.-G. Willinger, X.-P. Yang, Y. Jiang, T.-R. Zhang, X.-M. Meng, *Nanoscale* 7 (2015) 5311–5319.
- [38] K. Vinodgopal, I. Bedja, P.V. Kamat, *Chem. Mater.* 8 (1996) 2180–2187.
- [39] K.K. Akurati, A. Vital, R. Hany, B. Bommer, T. Graule, M. Winterer, *Int. J. Photoenergy* 7 (2005) 153–161.
- [40] M.T. Uddin, Y. Nicolas, C. Olivier, T. Toupance, L. Servant, M.M. Müller, H.-J. Kleebe, J.-R. Ziegler, W. Jaegermann, *Inorg. Chem.* 51 (2012) 7764–7773.
- [41] X. Xu, J. Zhuang, X. Wang, *J. Am. Chem. Soc.* 130 (2008) 12527–12535.
- [42] S.-K. Park, S.-H. Yu, N. Pinna, S. Woo, B. Jang, Y.-H. Chung, Y.-H. Cho, Y.-E. Sung, Y. Piao, *J. Mater. Chem.* 22 (2012) 2520–2525.
- [43] H. Zhu, D. Yang, G. Yu, H. Zhang, K. Yao, *Nanotechnology* 17 (2006) 2386.
- [44] Y. Kim, D.-J. Jang, *CrystEngComm* 16 (2014) 6989–6995.
- [45] Z. Liu, D.D. Sun, P. Guo, J.O. Leckie, *Nano Lett.* 7 (2007) 1081–1085.
- [46] S. Yan, D. Hu, F. Hu, J. Wu, N. Huang, Z. Xiao, *CrystEngComm* 13 (2011) 4580–4585.
- [47] Y.-P. Zhu, J. Li, T.-Y. Ma, Y.-P. Liu, G. Du, Z.-Y. Yuan, *J. Mater. Chem. A* 2 (2014) 1093–1101.
- [48] X. Zhang, J. Qin, Y. Xue, P. Yu, B. Zhang, L. Wang, R. Liu, *Sci. Rep.* 4 (2014) 4596.
- [49] P. Kundu, P.A. Deshpande, G. Madras, N. Ravishankar, *J. Mater. Chem.* 21 (2011) 4209–4216.
- [50] P. Guo, J. Jiang, S. Shen, L. Guo, *Int. J. Hydrogen Energy* 38 (2013) 13097–13103.
- [51] S. Hernaández, V. Cauda, A. Chiodoni, S. Dallorto, A. Sacco, D. Hidalgo, E. Celasco, C.F. Pirri, *ACS Appl. Mater. Interfaces* 6 (2014) 12153–12167.
- [52] K. Yu, S. Yang, H. He, C. Sun, C. Gu, Y. Ju, *J. Phys. Chem. A* 113 (2009) 10024–10032.
- [53] J. Lee, D.-J. Jang, *J. Phys. Chem. C* 120 (2016) 4130–4138.
- [54] D. Chen, H. Zhang, S. Hu, J. Li, *J. Phys. Chem. C* 112 (2008) 117–122.
- [55] X. Huang, L. Shang, S. Chen, J. Xia, X. Qi, X. Wang, T. Zhang, X.-M. Meng, *Nanoscale* 5 (2013) 3828–3833.
- [56] J. Lee, H.S. Shim, M. Lee, J.K. Song, D. Lee, *J. Phys. Chem. Lett.* 2 (2011) 2840–2845.
- [57] I.V. Lightcap, P.V. Kamat, *J. Am. Chem. Soc.* 134 (2012) 7109–7116.
- [58] J. Sun, H. Zhang, L.-H. Guo, L. Zhao, *ACS Appl. Mater. Interfaces* 5 (2013) 13035–13041.
- [59] K.-I. Ishibashi, A. Fujishima, T. Watanabe, K. Hashimoto, *Electrochem. Comm.* 2 (2000) 207–210.
- [60] Q. Xiang, D. Lang, T. Shen, F. Liu, *Appl. Catal. B: Environ.* 162 (2015) 196–203.